Micron 180 (2024) 103613

Contents lists available at ScienceDirect

Micron

journal homepage: www.elsevier.com/locate/micron

Full length article

EBSD investigation of microstructure and microtexture evolution on additively manufactured TiC-Fe based cermets—Influence of multiple laser scanning

H.S. Maurya [a,b,*], R.J. Vikram [c], R. Kumar [a], R. Rahmani [d,e], K. Juhani [a], F. Sergejev [a], K. G. Prashanth [a,f,g]

[a] Department of Mechanical and Industrial Engineering, Tallinn University of Technology, Ehitajate tee 5, Tallinn 19086, Estonia
[b] Luleå University of Technology, Department of Engineering Sciences and Mathematics, Luleå SE-97187, Sweden
[c] Department of Materials Engineering, Indian Institute of Science, Bangalore 560012, India
[d] CiTin– Centro de Interface Tecnológico Industrial, Arcos de Valdevez 4970-786, Portugal
[e] ProMetheus– Instituto Politécnico de Viana do Castelo (IPVC), Viana do Castelo 4900-347, Portugal
[f] Erich Schmid Institute of Materials Science, Austrian Academy of Sciences, Jahnstrasse 12, Leoben 8700, Austria
[g] CBCMT, School of Mechanical Engineering, Vellore Institute of TechnologyVellore, Tamil Nadu 630014, India

ARTICLE INFO

Keywords:
TiC-based cermets
Additive manufacturing
Electron backscatter diffraction
Microstructural characterization
Laser powder bed fusion

ABSTRACT

Sustainable TiC-Fe-based cermets have been fabricated by adopting an Additive Manufacturing route based on laser powder bed fusion technology (L-PBF). The objective is to produce crack-free cermet components by employing novel multiple laser scanning techniques with variations in laser process parameters. Electron backscatter diffraction analysis (EBSD) was used to study the microstructure and microtexture evolution with variations in laser process parameters. The investigation revealed that adjusting the preheating scan speed (PHS) and melting scan speed (MS) influenced the growth and nucleation of TiC phases. Lowering these speeds resulted in grain coarsening, while higher scan speeds led to grain refinement with larger sub-grain boundaries. Moreover, a high scanning speed increases the degree of dislocation density and internal stress in the fabricated cermet parts. Notably, it is revealed that decreasing the laser scan speed enhanced the proportion of high-angle grain boundaries in the cermet components, signifying an increase in material ductility.

1. Introduction

Cermets or cemented carbides are century-old ceramic-metal composites continuously employed in several machining, tunneling, and structural industries (Kang, 2014; Kübarsepp and Juhani, 2020). Owing to the high hardness and wear resistance of carbide particles (WC, TaC, NbC, TiC, etc.), and the excellent toughness of metallic binders such as (Co, Ni, and Fe, etc.) have gained cermets superiority always in demand (Mumtaz and Hopkinson, 2010; Anwer et al., 2023; Rajendhran et al., 2023). Additionally, the ability to tailor the carbide composition or introduction of duplex-carbides allows for customization to specific requirements, further enhancing their performance, especially in challenging impact-abrasion conditions (TBMs, etc) (Kang, 2014; Saha and Mallik, 2021a; Aramian, 2020). Traditionally, tungsten-based hard metals or cemented carbides have been extensively used. However, increasing prices and criticality involved with the raw materials supply, strict EU norms, and associated health risks with the disposal of tungsten and its binders such as cobalt, nickel, etc. have compelled industries to look for its alternative that is sustainable, green, and economical (Kübarsepp and Juhani, 2020; Tarraste et al., 2018).

To this end, titanium carbide-based cermets (TiC/Ti(C,N)-based), offer potential benefits such as being environmentally friendly, low-cost, and possessing superior mechanical and tribological properties at elevated temperatures (Kübarsepp and Juhani, 2020; Tarraste et al., 2018; Maurya et al., 2022a). Moreover, TiC-based cermets have received considerable attention ahead of conventional WC-Co/Ni/Fe-based cermets due to their lower density, tailor-ability to improved mechanical properties, wear-resistance, thermostability at temperatures up to 1800 °C, and laser-processibility (Zhuang et al., 2017; Li et al., 2010; Zhang et al., 2016; Cardinal et al., 2009; Maurya et al., 2022b). Additionally,

* Corresponding author at: Department of Mechanical and Industrial Engineering, Tallinn University of Technology, Ehitajate tee 5, Tallinn 19086, Estonia.
E-mail address: himanshu.singh.maurya@associated.ltu.se (H.S. Maurya).

https://doi.org/10.1016/j.micron.2024.103613
Received 19 December 2023; Received in revised form 20 February 2024; Accepted 20 February 2024
Available online 23 February 2024

when introduced with Fe-based binders, TiC-based composites offer an excellent sustainable choice for the replacement of toxic and critical binder elements (such as Co or Ni). Besides the high strength, low recycling cost, and further processing (heat treatment) ability of TiC-Fe-based cermets leads them ahead of their chart (Kübarsepp and Juhani, 2020; Maurya et al., 2022c). Furthermore, TiC-based cermets with Fe-based binders fabricated via an Additive manufacturing route hold promise for achieving sustainable development goals (SDGs 3, 7,8, 9,11, and 12) through the integration of three core elements (or systems) of sustainability i.e, economic growth, environmental protection, and social inclusion (Hatayama, 2022; Barbier and Burgess, 2021; Kumar et al., 2023).

Fabrication of these cermets via conventional processing routes such as Hot isostatic pressing (HIP), Hot pressing (HP), Spark plasma sintering (SPS, self-propagating high-temperature synthesis (SHS), etc., has limitations such as the creation of intricate designs, several post-processing steps, higher energy usage, longer processing time, high economy, etc., which can be overcome by advanced fabrication routes based on laser powder bed fusion (L-PBF)/Selective laser melting (SLM) (Bricin and Kriz, 2019; Olakanmi et al., 2015; Liu et al., 2021; Dareh Baghi et al., 2021). SLM is an Additive manufacturing (AM) process in which powder beds are selectively melted in a layer-by-layer fashion using a laser beam as a heat source to produce parts based on the CAD models. SLM offers a one-step fabrication of the parts with tunable microstructure and mechanical properties as compared to the conventional fabrication method.

There have been many efforts made to broaden the spectrum of materials used in laser-based additive manufacturing processes, including polymers, ceramics, metals, and their combinations, like cermets (Heydari et al., 2021; Frazier, 2014; Aramian et al., 2020; Yang et al., 2020; Kumar et al., 2020; Maurya et al., 2023a; Maurya, 2021; H. S. Maurya). Materials such as cermets or ceramic-metal composites pose the greatest challenge for laser-based additive manufacturing, due to their inherent brittle nature and variation in the thermal conductivity of the Ceramic and the binder phases. Moreover, the existence of unique and rapid solidification conditions of the L-PBF process imparts a high degree of internal stresses in the parts and a deterioration of its mechanical properties due to the formation of internal cracks (Waqar et al., 2022; Liu et al., 2011; Bian et al., 2020; K et al., 2021). To the best of our knowledge, there has been very scarce study regarding additive manufacturing of green TiC-Fe-based cermets and almost none towards the in-situ thermo-mechanical interaction that builds up during L-PBF of such ceramic-composites resulting in complex microstructural evolution and crystal orientations which may further affect the mechanical and tribological properties of such materials. The majority of previous studies have focused on WC and TiC-based cermets using Co/Ni-based binder systems (Aramian et al., 2020, 2021a; Zhao et al., 2022; Papy et al., 2023; Bjareborn, 2016; Xing et al., 2022; Li et al., 2022; Saha and Mallik, 2021b).

The current research encompasses a unique laser process parameter to reduce the thermal gradient during the fabrication of the cermets parts by adapting multiple laser scanning on the powder bed with variations in the laser parameter leading to the formation of parts with fine dendritic microstructures, reduced thermal cracks, and better mechanical properties. However, the influence of laser process parameters on the microstructural evolution during the SLM process of cermets has not been studied in detail. In addition, the SLM fabricated materials might exhibit anisotropy in the microstructure due to laser energy distribution, process parameters, and the morphology of the feedstock powders. Accordingly, here, an extensive EBSD analysis has been carried out to investigate the changes imparted by scan speed on the grain size, texture evolution, crystal orientation, grain boundary information, dislocation density, Schmid factor, etc. The research for the first time elaborates a detailed discussion of the in-situ microstructural features and micro-deformation mechanisms that generally operate in these cermets fabricated by L-PBF.

2. Material and methods

Initial feedstock powder of TiC (Pacific particulate materials Ltd.,1–3 μm, irregular) and ferritic stainless steel, AISI 430 L (Sandvik Osprey Ltd., 10–45 μm, spherical) has been mixed in the mechanical mixer for 24 h at 10 rpm with a 65:35 vol% ratio. SLM Realizer-50 device (ReaLizer GmbH, Borchen, Germany) equipped with pulsed Nd: YAG laser has been used for cermets fabrication. The optimized laser process parameters have been depicted in Table 1. A multiple laser scan strategy is being used to fabricate cermets parts with different laser energy densities/laser process parameters.

Two laser scans were performed on each layer of the powder bed in order to control the powder bed temperature and, thereby, residual stress formation. With the first laser scan, the powder bed is preheated using a high laser scan speed and low laser energy density, while the second laser scan uses a lower laser scan speed and high laser energy density to melt and fuse the powder particles (Fig. 1). A range of laser process parameters was employed to study the effects of laser energy density and scan speed on cermets fabrication (Table 1). Between two consecutive powder layers, a scanning rotation of 60° was employed. To minimize melt pool oxidation, an Argon atmosphere was used during fabrication in the building chamber, and the samples were built over a 316 L substrate plate.

A laser energy density (LED) is a measure of the effective amount of energy input per volume during LPBF/SLM (Prashanth, 2017).

$$LED = P/vhd \tag{1}$$

where P (in Watts) denotes the laser power, v (in mm/s) depicts the scanning velocity, h (in mm) represents the hatch distance, and d (in mm) the slice thickness of the individual layers.

To prepare the samples for microstructural analysis, standard hard metals procedures were followed. The microstructural analysis was done in a Carls Zeiss Gemini SEM 450 scanning electron microscope (SEM) in a backscattered electron (BSE) mode. Cermet samples for EBSD analysis have been prepared using a standard colloidal polishing method. Electron backscatter diffraction (EBSD) techniques were employed to understand the phase distribution, grain size, and other relevant parameters with the help of a high-velocity detector camera provided by Energy Dispersive X-ray analysis (EDAX). Using TSL OIM (TexSEM Laboratories-Orientation imaging microscopy) 8.1 software, an EBSD micrograph was taken at the step size of 0.2 μm with an operating voltage of 25 kV and a current of 12 nA. Phase analysis of the L-PBF fabricated parts was conducted by the Rigaku Smart lab X-Ray Diffractometer (XRD) with Cu-Kα radiation ($\lambda = 0.1542$ nm) at the room temperature within the scan range of 30–120° (2θ) and step size of 0.04°.

3. Results and discussion

XRD pattern of the TiC-Fe-based cermets with different laser process parameters has been depicted in Fig. 2. High-intensity peaks of TiC and α-Fe can be observed in the XRD analysis confirming that no additional

Table 1
Optimized laser process parameters for the fabrication of TiC-ferritic stainless steel using SLM: PHS – Pre-Heating Scan and MS – Melt Scan and H-SS – High-Scan Speed, M-SS – Medium-Scan Speed, and L-SS – Low-Scan Speed.

Specimen	Scan speed (mm/s)		Laser Energy density (LED) (J/mm^3)		Hatch distance (mm)	Layer thickness (mm)
	PHS	MS	PHS	MS		
H-SS	488	99	80	845	0.045	0.025
M-SS	203	81	84	959		
L-SS	176	56	97	1128		

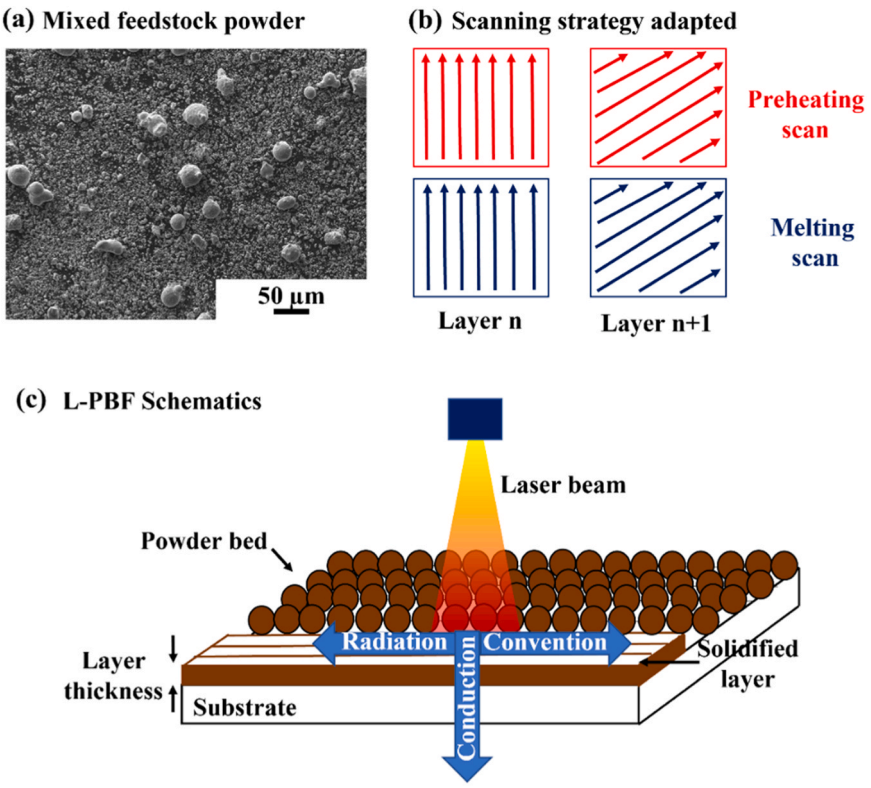

Fig. 1. (a) Scanning electron microscopy images of the mixed feedstock powder, (b) Schematics of scan strategy adapted for the fabrication of cermets, (c) Schematics of L-PBF process.

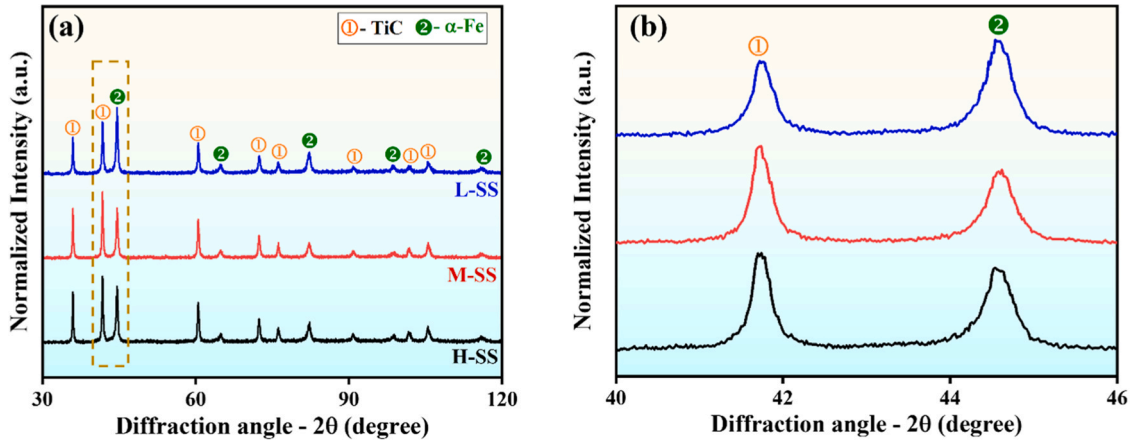

Fig. 2. X-ray diffraction patterns of L-PBF fabricated TiC-430 L based cermets (a) as-built parts with different laser process parameters, and (b) magnified view of the XRD peak.

phase (intermetallic carbides) formation has occurred during the fabrication process in all the as-built parts. However, both the observed phases may exhibit some minor changes in both peak intensity and broadening. Peak intensities may be related to the morphology of these samples (preferred orientation/growth) as a function of their preheating scan and melting scan energy densities (Maurya et al., 2022b; Ma et al., 2014). Adapting these variations in laser process parameters (PHS and MS) also caused a change in internal strain, which led to a broadening of peaks.

Fig. 3(a–c) exhibits the SEM microstructure of the TiC-based cermet with variation in the laser process parameters. It can be seen from the SEM micrograph that two distinct phases can be discerned, the black phases correspond to TiC, and the light gray areas are related to binder phases composed of Fe-Cr (AISI 430 L). Heterogeneous and anisotropic microstructure (finer and coarser) can be observed as a result of the multiple laser scanning adapted with different laser process parameters. The implementation of repetitive heating and cooling cycles coupled with a gradient of temperature during SLM is often responsible for creating such microstructural features. It is well known that four major parameters such as laser power, scan speed, hatch distance, and layer thickness are known to play a crucial role in the microstructural formation, densification, and defects during the LPBF process (According to Eq. 1). Consequently, variations in these laser process parameters modulated the microstructural characteristics of the fabricated parts.

A very fine microstructure was observed when faster scanning speeds for both preheating and melting scans were used (H-SS) (Fig. 3(a)). The

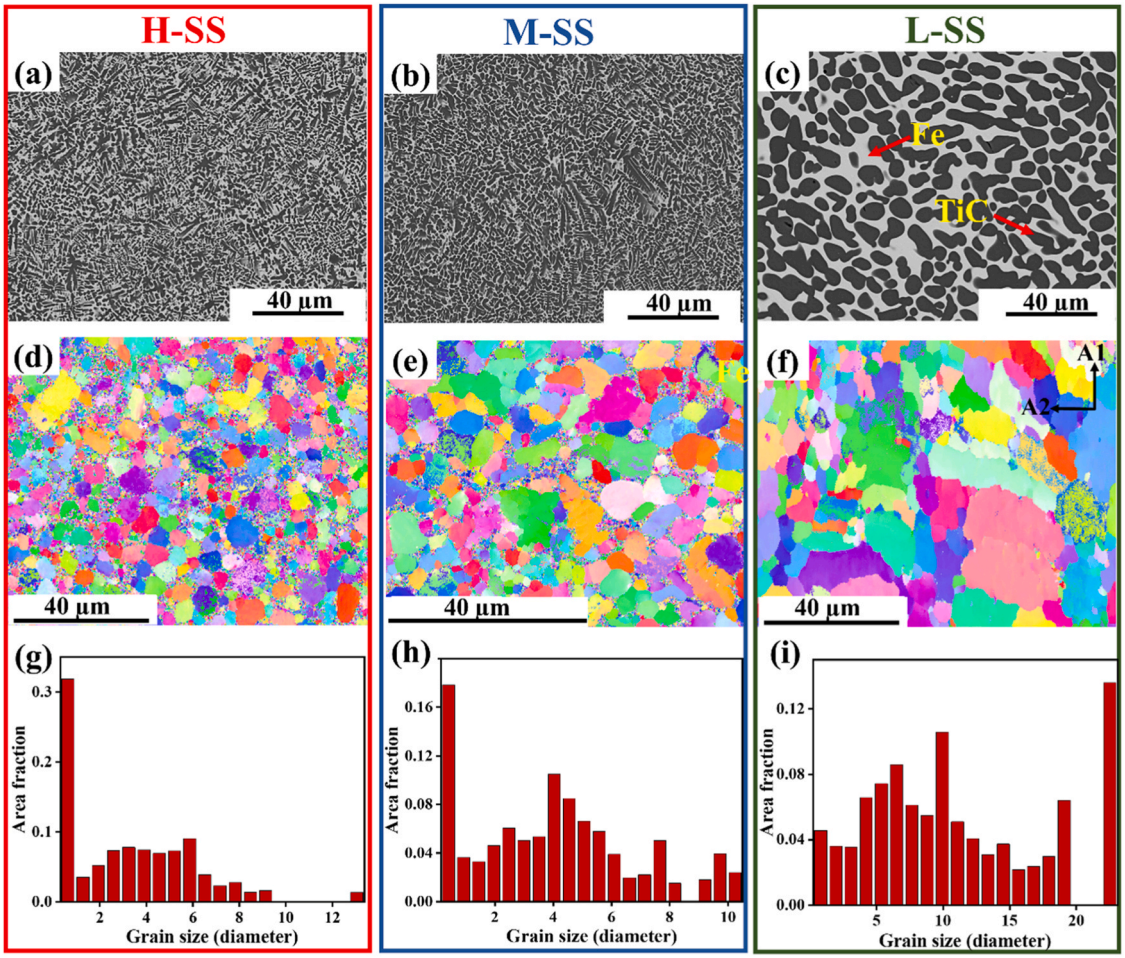

Fig. 3. BSE-SEM images of the TiC-based cermets with variation in laser process parameters (a) H-SS, (b) M-SS, and (c) L-SS. EBSD maps showing the grain size distribution in (d) H-SS, (e) M-SS, and (f) L-SS and their corresponding plots (g) H-SS, (h) M-SS, and (i) L-SS.

rapid solidification rate for the L-PBF process (up to 10^{6-8} K/s) may result in the development of these fine microstructures. It is also possible to relate this variation in microstructural formation (finer and coarser phases) to Gaussian laser energy distributions. The laser energy is more concentrated in the center of the melt pool and lower in the surrounding region when the laser is exposed to a powder bed. The inhomogeneous distribution of laser energy might be responsible for such wide thermal gradients in the melt pool and affect the microstructural characteristics. Marangoni convection and surface tension gradients are accordingly generated, causing molten materials to migrate from the pool center to the periphery (Xia et al., 2016). The molten materials sink under gravity at the pool edge, and then, owing to the buoyancy force caused by density difference, the fluid from the bottom floats up to the surface again (Sun et al., 2018). Moreover, this microstructural feature (fineness and shape) of the TiC phase could be influenced by the thermal gradient (G), solidification rate (R), and cooling rate of the melt pool ($T=G\times R$) (Aramian, 2020; Aramian et al., 2021b). This resulted in a finer microstructure due to the higher cooling rate at higher scan speeds and a coarser microstructure at lower scan speeds (Hooper, 2018; Li and Gu, 2014; Li et al., 2016; Singh et al., 2020).

During fabrication, reducing the scan speed (both PHS and MS) leads to coarsening of the TiC phase. The M-SS samples exhibit a coarser TiC phase with a lower gradient in the microstructure as compared to the H-SS sample (Fig. 3(b)). Typically, two different TiC phases (fine dendritic structures with refined dendritic arm lengths and coarser TiC phases with irregular shapes) can be observed in both the H-SS and M-SS samples (Fig. 3(a, b)).

However, further lowering the scanning speed led to coarsening and increased the lamellae thickness of the TiC phases (Fig. 3(c)). The coarser phases of TiC can be seen rather than dendritic phases, indicating a slower solidification/cooling rate. The coarsening of the phases during L-SS can be explained by the increment in the melt pool temperature, which affected the thermal gradient and solidification rate of the melt pool. Further, when the laser scans a fresh batch of powder during each layer of the printing process, the previously solidified layer has a heat conduction effect from the generated melt pool, causing coarsening of the microstructure.

The two competing phenomena, grain growth, and heterogeneous nucleation may be observed during the L-PBF, like in other rapid solidification processes (Kou, 2003). At the liquid-solid interface, grains grow rapidly when they are nucleated with a favorable crystallographic orientation (Aramian et al., 2021a; AlMangour et al., 2017; Calandri et al., 2019). Moreover, the epitaxial growth of these crystals is likely to preserve their crystallographic orientation. When a grain's crystallographic orientation differs from the preferred crystallographic orientation, epitaxial growth is inhibited. Therefore, heterogeneous nucleation dominates the solidification of molten material. A small number of large grains that are not restricted to melt pools appear despite dominant epitaxial growth. Contrary to this, heterogeneous nucleation processes result in a large number of small grains confined within melt pools. Epitaxial growth and heterogeneous nucleation are influenced by SLM process parameters, which alter the thermal flux in the melt pool. A dominant solidification mechanism in the fabricated parts appears to be heterogeneous nucleation, leading to random crystallographic

orientation.

A directional crystallographic orientation micrograph of TiC-based ceramics is shown in Fig. 3(d–f). In L-PBF, the temperature gradient reduces the nucleation rate at the solidification front, thereby promoting epitaxial grain growth as the preferred solidification mechanism. A significant variation in the grain size distribution may be observed with varying scanning speeds due to the adapted laser process parameters affecting the solidification/cooling rates during fabrication and the same may be observed from the mathematical plot shown in (Fig. 3 (g–i)). The H-SS samples exhibit finer grains with narrow distribution and more sub-grain with an average size of 3.3 μm. However, when lowering the scan speed of the M-SS sample increment in the overall grain size can be observed. In this case, a reduction in the finer grains can be observed with an increase in the average size of the grain (4.0 μm). For the lower scan speed sample (L-SS) coarser grain can be observed due to lower solidification/cooling rate. A wider grain size distribution is often observed in the SLM processed samples due to the Gaussian laser distribution and the anisotropic microstructural distribution caused by the complex thermal history and rapid cooling rate of the SLM components. The grain size observed in this case is 11 μm, which is over two times the size of H-SS and M-SS fabricated parts.

In the SLM process, the grain size of the fabricated parts is inversely proportional to the cooling rate. Moreover, grain morphology and texture also depend on the laser energy distribution, scan patterns, scan speed, heat transfer, etc (Akram et al., 2018; Chai et al., 2021). Temperature gradient, cooling rate, and crystal orientation all influence crystal growth, including size and orientation (Sun et al., 2018). In the initial stages of printing, more residual heat travels towards the substrate direction and surrounding powder layers (bottom) due to the heat conduction effect. Nucleating the grains is easy at this stage. Due to this, the growth is heavily influenced by the substrate, with smaller sizes and disorderly grain orientations. Following subsequent thermal cycling (STC), the cooling rate decreases as the accumulation reaches a certain height, resulting in an increase in grain size. Dendrite development is no longer influenced by the substrate. The solidification front will epitaxially follow an existing dendrite if the temperature gradient is similar to the gradient of the immediate next layer (Li et al., 2023). A similar trend of cooling rate can be established empirically based on the relationship between primary dendrite arm spacing (PDAS) and cooling rate shown in the following equation (Wang et al., 1992).

$$\alpha = 104.47 \times R^{-0.31} \quad (2)$$

.

where α and R denote primary dendrite arm spacing (in μm) and cooling rate (in °C/min), respectively.

Fig. 4(a–c) details the EBSD phase map of the SLM-fabricated TiC-Fe-based cermets with different laser process parameters. All the sample exhibits only two phases of TiC and α-Fe that corroborate with the XRD data. For the H-SS and M-SS samples, the region mostly consists of TiC and Fe phases with a similar area fraction of ≈70% and ≈30% respectively. However, in the case of the L-SS sample the region consists of a higher area fraction of TiC and a small amount of α-Fe phase. The lower volumetric phase of the binder phase could be attributed to the loss of the binder element such as Fe and Cr due to the slower heating rate and high laser energy density of the preheating and melting scan. As the laser energy density increases (L-SS), more binder elements such as Cr could be reduced due to their high vapor pressure and volatilization, leading to element loss in the binder phase (Kolnes et al., 2018). Fig. 4(d–f) exhibits the elemental distribution mapping of the TiC-Fe-based cermets with variations in laser process parameters. It can be observed that the distribution of the element of the TiC and binder phases was quite homogeneous in all three cases (H-SS, M-SS, and L-SS). No segregation of the elements can be observed in the L-PBF fabricated part formation suggesting that no formation of the unwanted intermetallic carbide formation has occurred in higher volume (corroborated with XRD analysis data). It has been reported, however, that conventional manufacturing processes such as Spark plasma sintering (SPS), liquid phase sintering (LPS), etc. lead to the formation of complex intermetallic carbides due to a slow heating rate in the process that leaves Cr-rich zones on the cermets parts, negatively affecting corrosion and toughness of the materials (Maurya et al., 2023a, 2023b; Kolnes et al., 2018). Adapting L-PBF, which offers high solidification and cooling rates, may overcome this disadvantage.

In the grain boundary maps and of the as-built specimen, the effect of the complex thermal history of the SLM can be observed on the grain boundary angle distribution (Fig. 5(a–f)). This map represents both low-angle grain and high-angle grain boundaries based on the color code. Red represents grain boundaries with low angles (LAGBs, θ < 15°), and

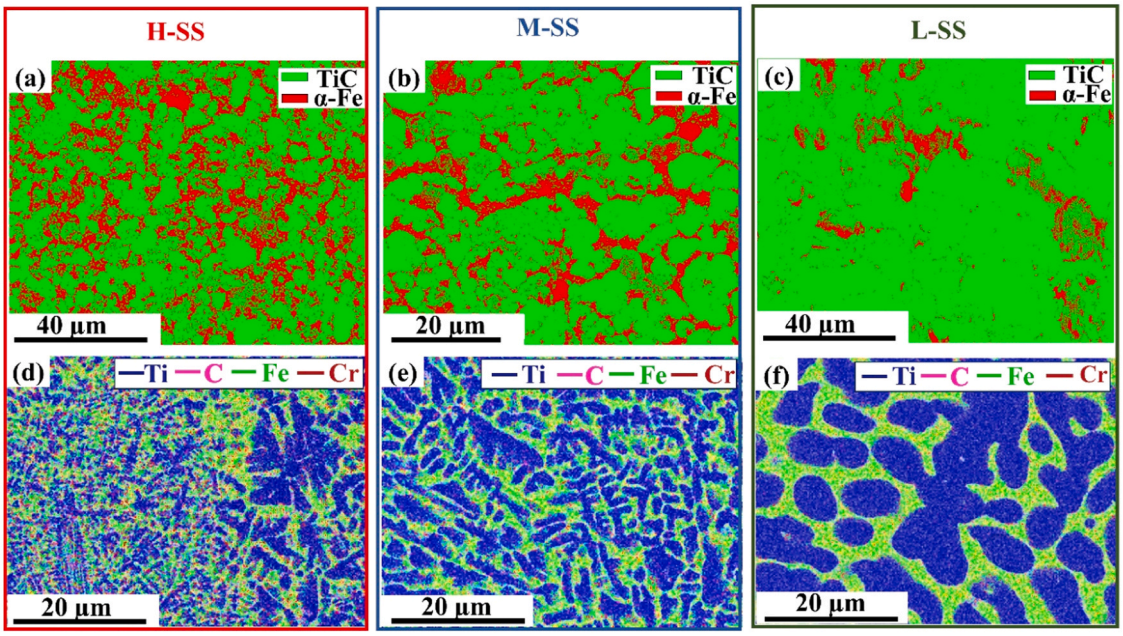

Fig. 4. EBSD phase diagram map (a) H-SS, (b) M-SS, and (c) L-SS and Elemental distribution map of the TiC-Fe based cermets fabricated via multiple laser scanning (d) H-SS, (e) M-SS, and (f) L-SS.

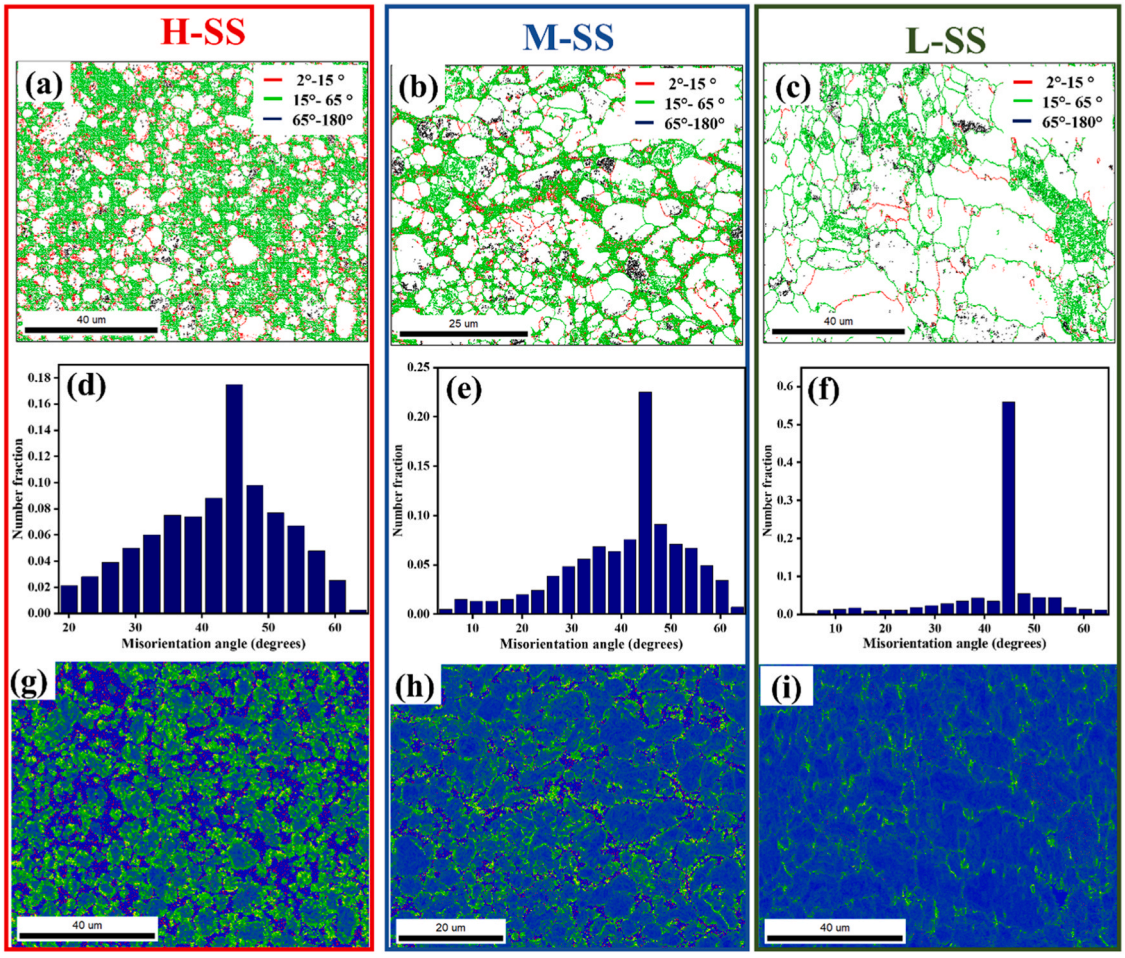

Fig. 5. EBSD grain boundary maps (a-c) and its misorientation distribution (d-f); Kernel average misorientation (KAM) maps of the SLM fabricated TiC-Fe based cermets (g-f).

green and blue color represents grain boundaries with high angles (HAGBs, θ > 65°). Sample with high and medium scan speed (H-SS and M-SS) exhibit a similar HAGBs and LAGBs fraction (56% and 13% respectively). Due to SLM's complex thermal history Higher melting/ Rapid solidification/ cooling rates lead to the formation of high dislocation density and dislocation wall resulting in a higher proportion of sub-grain fractions. HAGBs can be increased with a fraction of 60% in L-SS samples since larger grains are formed. Further, melting of the subsequent layer leads to reheating (Slow heating has a higher effect), which results in recrystallization and HAGB formation (Li et al., 2023; Wang et al., 1992). The misorientation angle can be utilized to characterize the strain distribution at the grain boundary of a deformed crystal material. This pattern can be described as a result of the accumulation of heat induced by layer-by-layer sedimentary accumulation, which increases the internal residual stress and grain boundary energy (K et al., 2021; Zhao et al., 2022), leading to an increase in grain boundary mobility.

The development of local strain as a function of changes in the laser process parameters has been studied using kernel average misorientation (KAM). The presence of Geometry Necessary Dislocation (GND) may be evaluated from KAM maps. In Fig. 5(g–i) a color band representing KAM values from 0 to 5° is shown on the map. A higher fraction of green color is characterized by a uniform distribution of dislocations, indicating higher dislocation density and more dislocation mobility (Li et al., 2019; Zhao et al., 2021). As a result of high laser scan speeds, high heating and cooling rates of the SLM process result in residual thermal stress accumulation, which increases dislocation density. Reducing the scan speed results in reducing the cooling rate leading to coarser grains and reduced dislocation density. In addition, strain accumulation takes place at the binder than TiC as a result of a mismatch between the coefficient of thermal expansion of the matrix and the binder. There is a correlation between higher laser scan speed (LSS), grain size, and differences in thermal coefficient expansion between TiC and the binder phase that led to higher dislocation density, higher thermal gradient, and residual stress formation (Toda-Caraballo et al., 2010; Jung et al., 2015). Thermal residual stress is reduced in the specimens if the scan speed is lowered, and the KAM average is lowered. The H-SS specimen's small grain size allows the accommodation of more strain and dislocations than a sample with large grain distribution due to fewer grain boundaries.

A representation of the Schmid factor map (SF) and grain orientation distribution of the as-built specimen can be seen in (Fig. 6). The specimens were measured in the same areas as the IPF maps to determine grain orientation distribution. SF maps play an important role in determining a material's properties, especially measuring the plastic deformation ability of material concerning a given slip system. According to Schmid's law, the yield strength of a material can be calculated on a macro level using the formula below (Hosford, 2005).

$$\tau_c = \sigma_s \cos\lambda \quad \cos \quad \varphi \tag{3}$$

where $\cos\lambda\cos\varphi$denotes the Schmid factor (SF), τ_c denotes the intrinsic coefficient of materials, which is determined by the material itself, and σ_s refer to the yield strength of the material. The material will not deform plastically until the shear stress in the slip plane and slip di-

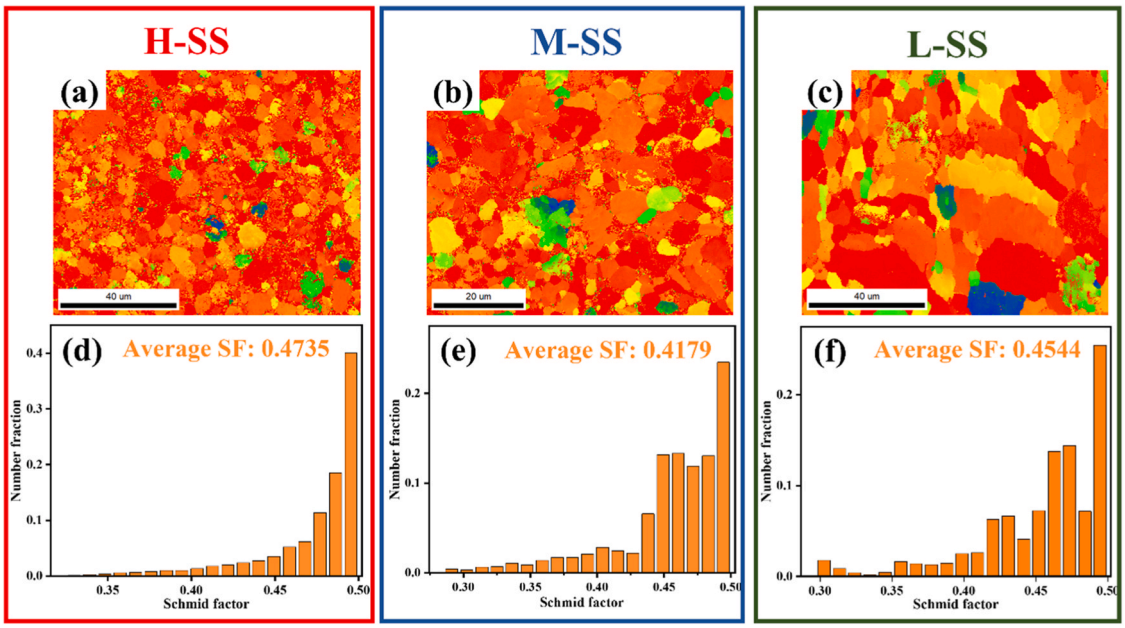

Fig. 6. Schmid factor maps and their distribution profile observed for the TiC-based cermets fabricated by selective laser melting, (a, d) H-SS, (b, e) M-SS, and (c, f) L-SS.

rection reaches a critical value, i.e., when the slip system is operable. This results in lower yield strength, higher ductility, and toughness when the Schmid factor is higher (Aramian et al., 2021a; Li et al., 2019; Chen et al., 2018). As the SF value increases, the shear stress resolves more readily, allowing the slip system to operate more effectively with the applied force (Ullah et al., 2021). Consequently, high SF results in lower yield stress and higher ductility and toughness for the as-built specimens (Li et al., 2019). A maximum SF of 0.4735 has been achieved for the H-SS specimen. The present results suggest that the ability of the bimodal microstructure (finer dendritic and coarser phase) of the cermets decreases with decreasing laser scan speed due to Gaussian laser energy distribution and employment of the multiple scan strategy. A micro-melt pool is formed when laser and powder particles interact, creating more complex local melt conditions, such as Benard-Marangoni instability with repetitive heating and cooling cycles (Kong et al., 2021; Kan et al., 2021). (Fig. 6(d-f)). Having a lower scan speed leads to higher temperatures in the center of the melt pool and causes a gradient in energy in the melt pool and its surroundings.

Pole figures were used to track the evolution of crystallographic textures. Fig. 7 shows the pole figures for the TiC and α-Fe phases in the as-built SLM specimens as a function of changes in the LSS. It can be observed that all the specimens show a strong texture intensity in the (001) pole figure compared to other directions. The texture strength lies in the A1 direction for the H-SS and M-SS while for the L-SS the texture strength lies in the A2 direction. The SLM process leads to non-equilibrium solidification conditions resulting in such changes in texture. The texture intensity of the TiC in all the specimens increases with a decrease in LSSs 2.04, 2.47, and 4.43, for the H-SS, M-SS, and L-SS samples respectively. α-Fe texture intensity also follows the same trend (2.8, 4.15, and 9.559). This increment in the intensity indicates the TiC and α-Fe phase texture is enhanced by lowering the scan speed. The lack of obvious dominant texture and disorder arrangement in the pole figure can be explained by a thermal gradient in the melt pool due to Gaussian laser energy distribution and laser scan rotation (60°) that can affect the preferred solidification direction along with the complex and unique SLM solidification conditions (Wang et al., 2015, 2021

4. Conclusion

In the present study, we have investigated the evolution of microstructure and microtexture during the 3D fabrication of a TiC-Fe-based cermet by varying the laser scan speed. The following conclusions can be drawn from this research:

(1) It is observed that reducing both the preheating scan (PHS) and melting scan (MS) speed results in an increase in the melt pool temperature, causing grain coarsening. This, in turn, leads to decreased dislocation density and reduced internal stresses in the material. In contrast, higher PHS and MS can result in increased dislocation densities and a higher degree of internal stresses in the cermets as a result of rapid melting and solidification.
(2) The gradient (coarse and fine grain) in the microstructure of the cermets increases with elevated scan speed suggesting that the material fabricated at lower scan speeds may exhibit higher ductility.
(3) The intensity of the texture of both TiC and the binder phase also increases with reducing scan speed. A lower scan speed leads to reduced texture thereby contributing to improved ductility in the material.

Author's disclosure statement

The authors declare that they have no known competing financial interests or personal relationships that could have appeared to influence the work reported in this paper.

CRediT authorship contribution statement

Himanshu Singh Maurya: Writing – review & editing, Writing – original draft, Resources, Investigation, Data curation, Conceptualization. **K.G. Prashanth:** Writing – review & editing, Supervision, Resources, Funding acquisition. **F. Sergejev:** Writing – review & editing, Supervision, Funding acquisition. **K. Juhani:** Writing – review & editing, Visualization, Resources, Funding acquisition. **R. Rahmani:** Writing – review & editing. **R. Kumar:** Writing – review & editing, Investigation. **R. J. Vikram:** Visualization, Investigation, Data curation.

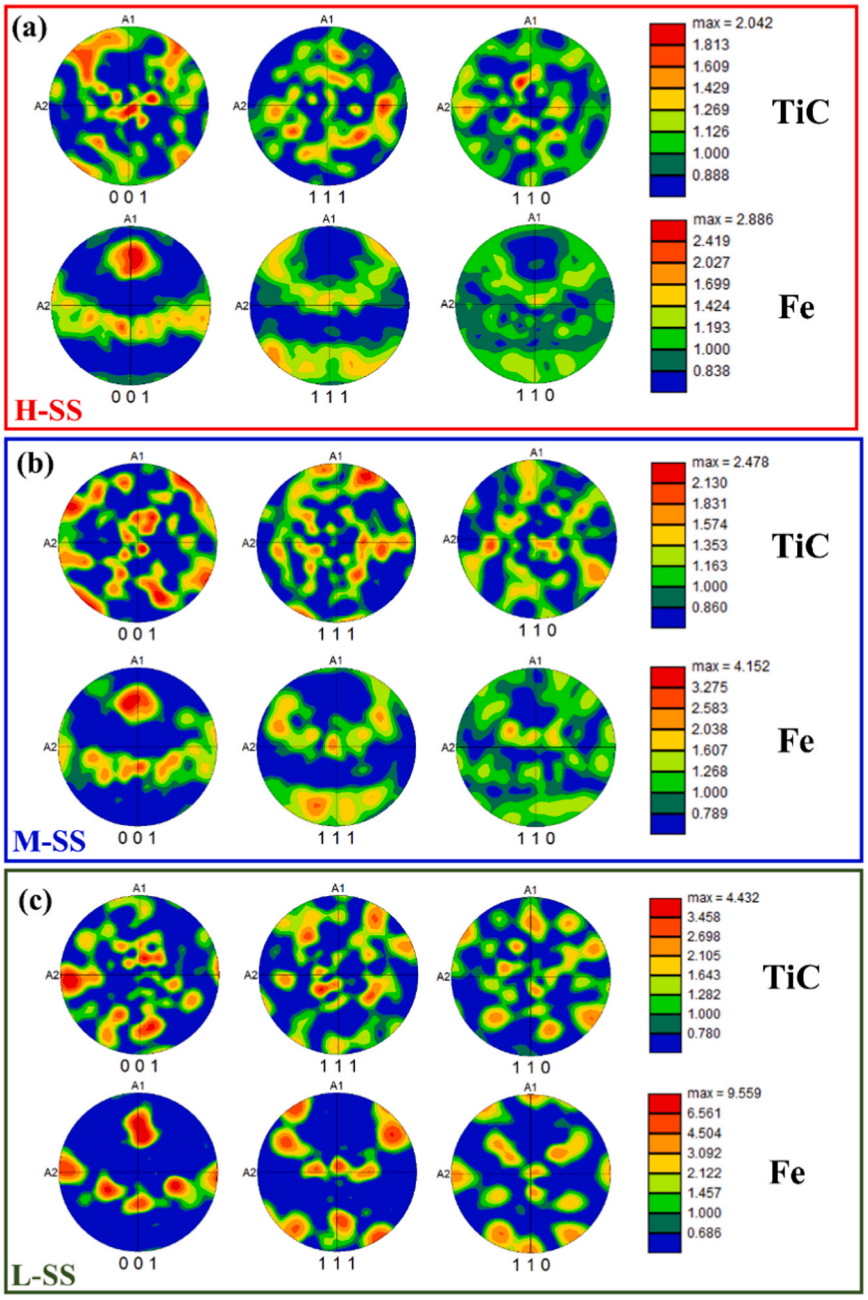

Fig. 7. Evaluation of the texture evolution in the TiC-Fe-based cermets by pole figure as a function of LSS (a) H-SS, (b) M-SS, and (c) L-SS.

Declaration of Competing Interest

The authors declare that they have no known competing financial interests or personal relationships that could have appeared to influence the work reported in this paper.

Data availability

Data will be made available on request.

Acknowledgments

This work was supported by Estonian Research Council grant no. PRG1145 “Composites ‘ceramic-Fe-alloy’ for a wide range of application conditions”, M-ERA. Net project “DuplexCER” MNHA22040 and European Regional Development Grant ASTRA6–6.

References

Akram, J., Chalavadi, P., Pal, D., Stucker, B., 2018. Understanding grain evolution in additive manufacturing through modeling. Addit. Manuf. 21, 255–268. https://doi.org/10.1016/j.addma.2018.03.021.

AlMangour, B., Grzesiak, D., Yang, J.M., 2017. In-situ formation of novel TiC-particle-reinforced 316L stainless steel bulk-form composites by selective laser melting. J. Alloy. Compd. 706, 409–418. https://doi.org/10.1016/j.jallcom.2017.01.149.

Anwer, Z., Vleugels, J., Datye, A., Zhang, S., Huang, S., 2023. Influence of varying carbon content in (V,Nb,Ta,Ti,W)C high entropy carbide - Ni based cermets on densification, microstructure, mechanical properties and phase stability. Ceram. Int 49, 4997–5012. https://doi.org/10.1016/j.ceramint.2022.11.121.

Aramian, A., 2020. Effect of selective laser melting process parameters on microstructural and mechanical properties of TiC–NiCr cermet. Ceram. Int 46, 28749–28757. https://doi.org/10.1016/j.ceramint.2020.08.037.

Aramian, A., Razavi, S.M.J., Sadeghian, Z., Berto, F., 2020. A review of additive manufacturing of cermets. Addit. Manuf. 33, 101130 https://doi.org/10.1016/j.addma.2020.101130.

Aramian, A., Sadeghian, Z., Wan, D., Holovenko, Y., Razavi, S.M.J., Berto, F., 2021b. Microstructure and texture evolution during the manufacturing of in situ TiC-NiCr

cermet through selective laser melting process. Mater. Charact. 178, 111289 https://doi.org/10.1016/j.matchar.2021.111289.
Aramian, A., Sadeghian, Z., Wan, D., Holovenko, Y., Razavi, S.M.J., Berto, F., 2021a. Microstructure and texture evolution during the manufacturing of in situ TiC-NiCr cermet through selective laser melting process. Mater. Charact. 178, 111289 https://doi.org/10.1016/j.matchar.2021.111289.
Barbier, E.B., Burgess, J.C., 2021. In: The SDGs and the Systems Approach to Sustainability BT - Economics of the SDGs: Putting the Sustainable Development Goals into Practice. Springer International Publishing, Cham, pp. 15–37. https://doi.org/10.1007/978-3-030-78698-4_2.
Bian, P., Shi, J., Liu, Y., Xie, Y., 2020. Influence of laser power and scanning strategy on residual stress distribution in additively manufactured 316L steel. Opt. Laser Technol. 132, 106477 https://doi.org/10.1016/j.optlastec.2020.106477.
Oscar Bjareborn, WC grain size distribution during sintering of WC-Co cemented carbides, (2016).
Bricin, D., Kriz, A., 2019. Processability of WC-CO powder mixtures using slm additive technology. MM Sci. J. 2019, 2939–2944. https://doi.org/10.17973/MMSJ.2019_06_2018115.
Calandri, M., Yin, S., Aldwell, B., Calignano, F., Lupoi, R., Ugues, D., 2019. Texture and microstructural features at different length scales in inconel 718 produced by selective laser melting. Mater. (Basel) 12. https://doi.org/10.3390/ma12081293.
Cardinal, S., Malchère, A., Garnier, V., Fantozzi, G., 2009. Microstructure and mechanical properties of TiC-TiN based cermets for tools application. Int J. Refract Met Hard Mater. 27, 521–527. https://doi.org/10.1016/j.ijrmhm.2008.10.006.
Chai, R., Zhang, Y., Zhong, B., Zhang, C., 2021. Effect of scan speed on grain and microstructural morphology for laser additive manufacturing of 304 stainless steel, 60, 744–760. https://doi.org/10.1515/rams-2021-0068.
Chen, Z., Chen, S., Wei, Z., Zhang, L., Wei, P., Lu, B., Zhang, S., Xiang, Y., 2018. Anisotropy of nickel-based superalloy K418 fabricated by selective laser melting. Prog. Nat. Sci. Mater. Int 28, 496–504. https://doi.org/10.1016/j.pnsc.2018.07.001.
Dareh Baghi, A., Nafisi, S., Hashemi, R., Ebendorff-Heidepriem, H., Ghomashchi, R., 2021. Effective post processing of SLM fabricated Ti-6Al-4 V alloy: machining vs thermal treatment. J. Manuf. Process 68, 1031–1046. https://doi.org/10.1016/j.jmapro.2021.06.035.
Frazier, W.E., 2014. Metal additive manufacturing: a review. J. Mater. Eng. Perform. 23, 1917–1928. https://doi.org/10.1007/s11665-014-0958-z.
Hatayama, H., 2022. The metals industry and the sustainable development goals: the relationship explored based on SDG reporting. Resour. Conserv Recycl 178, 106081. https://doi.org/10.1016/j.resconrec.2021.106081.
Heydari, L., Lietor, P.F., Corpas-Iglesias, F.A., Laguna, O.H., 2021. Ti(C,n) and wc-based cermets: a review of synthesis, properties and applications in additive manufacturing. Mater. (Basel) 14. https://doi.org/10.3390/ma14226786.
Hooper, P.A., 2018. Melt pool temperature and cooling rates in laser powder bed fusion. Addit. Manuf. 22, 548–559. https://doi.org/10.1016/j.addma.2018.05.032.
W.F. Hosford, Mechanical Behavior of Materials, Cambridge University Press, Cambridge, 2005. https://doi.org/DOI: 10.1017/CBO9780511810930.
Jung, H.Y., Choi, S.J., Prashanth, K.G., Stoica, M., Scudino, S., Yi, S., Kühn, U., Kim, D.H., Kim, K.B., Eckert, J., 2015. Fabrication of Fe-based bulk metallic glass by selective laser melting: a parameter study. Mater. Des. 86, 703–708. https://doi.org/10.1016/j.matdes.2015.07.145.
K, N.B., K, V., Tigga, A.K., Barad, S., S, A.K., 2021. Influence of post-processing techniques on residual stresses of SLM processed HPNGV. J. Manuf. Process 66, 189–197. https://doi.org/10.1016/j.jmapro.2021.04.020.
Kan, X., Yin, Y., Yang, D., Li, W., Sun, J., 2021. Micro pool characteristics of 316L and the influence of sulfur during SLM. Opt. Laser Technol. 142, 107136 https://doi.org/10.1016/j.optlastec.2021.107136.
S. Kang, Cermets, 2014. https://doi.org/10.1016/B978-0-08-096527-7.00005-2.
Kolnes, M., Mere, A., Kübarsepp, J., Viljus, M., Maaten, B., Tarraste, M., 2018. Microstructure evolution of TiC cermets with ferritic AISI 430L steel binder. Powder Met. 61, 197–209. https://doi.org/10.1080/00325899.2018.1447268.
Kong, D., Dong, C., Wei, S., Ni, X., Zhang, L., Li, R., Wang, L., Man, C., Li, X., 2021. About metastable cellular structure in additively manufactured austenitic stainless steels. Addit. Manuf. 38, 101804 https://doi.org/10.1016/j.addma.2020.101804.
Kou, S., 2003. Welding Metallurgy.
Kübarsepp, J., Juhani, K., 2020. Cermets with Fe-alloy binder: a review. Int J. Refract Met Hard Mater. 92, 105290 https://doi.org/10.1016/j.ijrmhm.2020.105290.
Kumar, R., Antonov, M., Beste, U., Goljandin, D., 2020. Assessment of 3D printed steels and composites intended for wear applications in abrasive, dry or slurry erosive conditions. Int. J. Refract Met Hard Mater. 86, 105126 https://doi.org/10.1016/j.ijrmhm.2019.105126.
Kumar, R., Kariminejad, A., Antonov, M., Goljandin, D., Klimczyk, P., Hussainova, I., 2023. Progress in sustainable recycling and circular economy of tungsten carbide hard metal scraps for industry 5.0 and Onwards. Sustainability 15. https://doi.org/10.3390/su151612249.
Li, B., Liu, Y., Li, J., Cao, H., He, L., 2010. Effect of sintering process on the microstructures and properties of in situ TiB2–TiC reinforced steel matrix composites produced by spark plasma sintering. J. Mater. Process Technol. 210, 91–95. https://doi.org/10.1016/j.jmatprotec.2009.08.008.
Li, K., Wei, L., An, B., Yu, B., Misra, R.D.K., 2019. Aging phenomenon in low lattice-misfit cobalt-free maraging steel: Microstructural evolution and strengthening behavior. Mater. Sci. Eng. A 739, 445–454. https://doi.org/10.1016/j.msea.2018.10.069.
Li, L., Liu, F., Nie, S., Wang, Q., Zhao, R., Zhang, Y., Feng, H., Lin, X., 2023. Effect of thermal cycling on grain evolution and micro-segregation in selective laser melting of FGH96 superalloy. Metals 13. https://doi.org/10.3390/met13010121.
Li, X., Zhao, Y., Guo, Z., Liu, Y., Wang, H., Zhang, J., Yi, D., Cao, Y., Yang, X., Liu, B., Liu, Y., Bai, P., 2022. Influence of different substrates on the microstructure and mechanical properties of WC-12Co cemented carbide fabricated via laser melting deposition. Int J. Refract Met Hard Mater. 104, 105787 https://doi.org/10.1016/j.ijrmhm.2022.105787.
Li, X.P., O'Donnell, K.M., Sercombe, T.B., 2016. Selective laser melting of Al-12Si alloy: enhanced densification via powder drying. Addit. Manuf. 10, 10–14. https://doi.org/10.1016/j.addma.2016.01.003.
Li, Y., Gu, D., 2014. Parametric analysis of thermal behavior during selective laser melting additive manufacturing of aluminum alloy powder. Mater. Des. 63, 856–867. https://doi.org/10.1016/j.matdes.2014.07.006.
Liu, B., Fang, G., Lei, L., 2021. An analytical model for rapid predicting molten pool geometry of selective laser melting (SLM). Appl. Math. Model 92, 505–524. https://doi.org/10.1016/j.apm.2020.11.027.
Liu, F., Lin, X., Yang, G., Song, M., Chen, J., Huang, W., 2011. Microstructure and residual stress of laser rapid formed Inconel 718 nickel-base superalloy. Opt. Laser Technol. 43, 208–213. https://doi.org/10.1016/j.optlastec.2010.06.015.
Ma, P., Prashanth, K.G., Scudino, S., Jia, Y., Wang, H., Zou, C., Wei, Z., Eckert, J., 2014. Influence of annealing on mechanical properties of Al-20Si processed by selective laser melting. Met. (Basel) 4, 28–36. https://doi.org/10.3390/met4010028.
Maurya, 2021. Additive manufacturing of TiC-based cermet with stainless steel as a binder material. Mater. Today Proc.
H.S. Maurya, Additive Manufacturing of TiC-based Cermets with Fe-based Binders using Novel Laser Scan Techniques, TalTech Press, n.d. https://doi.org/https://doi.org/10.23658/taltech.61/2023.
Maurya, H.S., Juhani, K., Sergejev, F., Prashanth, K.G., 2022b. Additive manufacturing of TiC-based cermet with stainless steel as a binder material. Mater. Today Proc. 57, 824–828. https://doi.org/10.1016/j.matpr.2022.02.428.
Maurya, H.S., Kollo, L., Juhani, K., Sergejev, F., Prashanth, K.G., 2022a. Effect of preheating and cooling of the powder bed by laser pulse shaping on the microstructure of the TiC based cermets. Ceram. Int. https://doi.org/10.1016/j.ceramint.2022.04.029.
Maurya, H.S., Kollo, L., Tarraste, M., Juhani, K., Sergejev, F., Prashanth, K.G., 2022c. Effect of the Laser Processing Parameters on the Selective Laser Melting of TiC–Fe-Based Cermets. J. Manuf. Mater. Process 6. https://doi.org/10.3390/jmmp6020035.
Maurya, H.S., Jayaraj, J., Wang, Z., Juhani, K., Sergejev, F., Prashanth, K.G., 2023b. Investigation of the tribological behavior of the additively manufactured TiC-based cermets by scratch testing. J. Alloy. Compd. 959, 170496 https://doi.org/10.1016/j.jallcom.2023.170496.
Maurya, H.S., Jayaraj, J., Vikram, R.J., Juhani, K., Sergejev, F., Prashanth, K.G., 2023a. Additive manufacturing of TiC-based cermets: A detailed comparison with spark plasma sintered samples. J. Alloy. Compd. 960, 170436 https://doi.org/10.1016/j.jallcom.2023.170436.
Mumtaz, K., Hopkinson, N., 2010. Selective laser melting of Inconel 625 using pulse shaping. Rapid Prototyp. J. 16, 248–257. https://doi.org/10.1108/13552541011049261.
Olakanmi, E.O., Cochrane, R.F., Dalgarno, K.W., 2015. A review on selective laser sintering/melting (SLS/SLM) of aluminium alloy powders: Processing, microstructure, and properties. Prog. Mater. Sci. 74, 401–477. https://doi.org/10.1016/j.pmatsci.2015.03.002.
Papy, K., Borbely, A., Sova, A., Favre, J., Bertrand, P., Staerck, J.M., 2023. Additive manufacturing of cermet produced by laser powder bed fusion using alternative Ni binder. Mater. Res Proc. 28, 129–138. https://doi.org/10.21741/9781644902479-15.
Prashanth, K.G., 2017. Is the energy density a reliable parameter for materials synthesis by selective laser melting? Mater. Res Lett. 5, 386–390. https://doi.org/10.1080/21663831.2017.1299808.
Rajendhran, N., Pondicherry, K., Huang, S., Vleugels, J., De Baets, P., 2023. Influence of abrasive characteristics on the wear micro-mechanisms of NbC and WC cermets during three-body abrasion. Wear 530–531, 205007. https://doi.org/10.1016/j.wear.2023.205007.
Saha, M., Mallik, M., 2021b. Additive manufacturing of ceramics and cermets: present status and future perspectives. Sādhanā 46, 162. https://doi.org/10.1007/s12046-021-01685-2.
Saha, M., Mallik, M., 2021a. Additive manufacturing of ceramics and cermets: present status and future perspectives. Sādhanā 46, 162. https://doi.org/10.1007/s12046-021-01685-2.
Singh, N., Hameed, P., Ummethala, R., Manivasagam, G., Prashanth, K.G., Eckert, J., 2020. Selective laser manufacturing of Ti-based alloys and composites: impact of process parameters, application trends, and future prospects. Mater. Today Adv. 8, 100097 https://doi.org/10.1016/j.mtadv.2020.100097.
Sun, S.-H., Hagihara, K., Nakano, T., 2018. Effect of scanning strategy on texture formation in Ni-25at%Mo alloys fabricated by selective laser melting. Mater. Des. 140, 307–316. https://doi.org/10.1016/j.matdes.2017.11.060.
Tarraste, M., Kübarsepp, J., Juhani, K., Mere, A., Kolnes, M., Viljus, M., Maaten, B., 2018. Ferritic chromium steel as binder metal for WC cemented carbides. Int J. Refract Met Hard Mater. 73, 183–191. https://doi.org/10.1016/j.ijrmhm.2018.02.010.
Toda-Caraballo, I., Chao, J., Lindgren, L.E., Capdevila, C., 2010. Effect of residual stress on recrystallization behavior of mechanically alloyed steels. Scr. Mater. 62, 41–44. https://doi.org/10.1016/j.scriptamat.2009.09.023.
Ullah, R., Lu, J., Sang, L., Rizwan, M., Zhang, Y., Zhang, Z., 2021. Investigating the microstructural evolution during deformation of laser additive manufactured Ti–6Al–4V at 400 °C using in-situ EBSD. Mater. Sci. Eng. A 823, 141761. https://doi.org/10.1016/j.msea.2021.141761.
Wang, H.M., Zhang, J.H., Tang, Y.J., Hu, Z.Q., Yukawa, N., Morinaga, M., Murata, Y., 1992. Rapidly solidified MC carbide morphologies of a laser-glazed single-crystal nickel-base superalloy. Mater. Sci. Eng. A 156, 109–116. https://doi.org/10.1016/0921-5093(92)90421-V.

Wang, Z., Qu, R.T., Scudino, S., Sun, B.A., Prashanth, K.G., Louzguine-Luzgin, D.V., Chen, M.W., Zhang, Z.F., Eckert, J., 2015. Hybrid nanostructured aluminum alloy with super-high strength. NPG Asia Mater. 7 https://doi.org/10.1038/am.2015.129.

Wang, Z., Tang, S.Y., Scudino, S., Ivanov, Y.P., Qu, R.T., Wang, D., Yang, C., Zhang, W. W., Greer, A.L., Eckert, J., Prashanth, K.G., 2021. Additive manufacturing of a martensitic Co–Cr–Mo alloy: Towards circumventing the strength–ductility trade-off. Addit. Manuf. 37, 101725 https://doi.org/10.1016/j.addma.2020.101725.

Waqar, S., Guo, K., Sun, J., 2022. Evolution of residual stress behavior in selective laser melting (SLM) of 316L stainless steel through preheating and in-situ re-scanning techniques. Opt. Laser Technol. 149, 107806 https://doi.org/10.1016/j.optlastec.2021.107806.

Xia, M., Gu, D., Yu, G., Dai, D., Chen, H., Shi, Q., 2016. Selective laser melting 3D printing of Ni-based superalloy: understanding thermodynamic mechanisms. Sci. Bull. 61, 1013–1022. https://doi.org/10.1007/s11434-016-1098-7.

Xing, M., Wang, H., Zhao, Z., Zhang, Y., Lou, H., Liu, C., Wang, M., Song, X., 2022. SLM printing of cermet powders: Inhomogeneity from atomic scale to microstructure. Ceram. Int. https://doi.org/10.1016/j.ceramint.2022.06.254.

Yang, Y., Zhang, C., Wang, D., Nie, L., Wellmann, D., Tian, Y., 2020. Additive manufacturing of WC-Co hardmetals: a review. Int J. Adv. Manuf. Technol. 108, 1653–1673. https://doi.org/10.1007/s00170-020-05389-5.

Zhang, C., Du, Y., Zhou, S., Peng, Y., Wang, J., 2016. Grain growth and hardness of TiC-based cermets: Experimental investigation and thermodynamic calculations. Ceram. Int 42, 19289–19295. https://doi.org/10.1016/j.ceramint.2016.09.096.

Zhao, C., Wang, Z., Li, D., Kollo, L., Luo, Z., Zhang, W., Gokuldoss, K., Prashanth, K.G., 2021. Selective laser melting of Cu – Ni – Sn: A comprehensive study on the microstructure, mechanical properties, and deformation behavior. Int J. Plast. 138, 102926 https://doi.org/10.1016/j.ijplas.2021.102926.

Zhao, Y., Wang, H., Zhang, L., Li, X., Guo, Z., Zhang, J., Yi, D., Liu, B., Bai, P., 2022. Study on the microstructure and properties of WC-12Co cemented carbide fabricated by selective laser melting. J. Mater. Res Technol. 20, 3512–3521. https://doi.org/10.1016/j.jmrt.2022.08.082.

Zhuang, Q., Lin, N., He, Y., Kang, X., 2017. Influence of temperature on sintering behavior and properties of TiC-Fe-Co-Ni-Cr-Mo cermets. Ceram. Int 43, 15992–15998. https://doi.org/10.1016/j.ceramint.2017.08.186.